Submitted to

International Europhysics Conference on High Energy Physics, July 12, 2001, Budapest
EPS 2001: Abstract: **808**
Parallel Session **2**

XX International Symposium on Lepton and Photon Interactions, July 23, 2001, Rome
LP 2001: Abstract: **500**
Plenary Session **8**

www-h1.desy.de/h1/www/publications/conf/conf_list.html

Measurement of the Diffractive Structure Function $F_2^{D(3)}(\beta, Q^2, x_{I\!P})$ at HERA

H1 Collaboration

Abstract

A new high precision inclusive measurement of the diffractive deep inelastic scattering (DIS) process $ep \to eXY$ is presented, where Y is a proton or a low mass proton excitation carrying a fraction $1 - x_{I\!P} > 0.95$ of the beam longitudinal momentum and the squared 4-momentum transfer at the proton vertex $t > -1$ GeV^2. The measurement is presented in the form of a diffractive structure function $F_2^{D(3)}(\beta, Q^2, x_{I\!P})$, which is measured in the kinematic range $6.5 < Q^2 < 120\ \mathrm{GeV}^2$, $0.01 < \beta < 0.9$ and $10^{-4} \lesssim x_{I\!P} < 0.05$. The $x_{I\!P}$ dependence of the data is interpreted in terms of a measurement of the effective pomeron intercept $\alpha_{I\!P}(0)$, which is compared with the same quantity extracted from inclusive DIS. The β and Q^2 dependences of F_2^D are studied at fixed $x_{I\!P}$. Scaling violations resulting in a rising dependence on $\ln Q^2$ are observed up to large values of β. The Q^2 dependence of F_2^D is compared with the Q^2 dependence of $F_2(x, Q^2)$ at the same value of x. The data can be described by the DGLAP evolution equations assuming QCD hard scattering factorisation for semi-inclusive processes and an $x_{I\!P}$ dependence motivated by Regge theory. The measured F_2^D is compared with models for diffractive DIS.

1 Introduction

The description of diffractive Deep-Inelastic Scattering (DIS) has become one of the main challenges in the development of our understanding of Quantum Chromodynamics (QCD). The presence of large gaps in the rapidity distribution of final state hadrons implies the exchange of systems of at least two partons in a net colour singlet configuration and therefore requires new field theory techniques for a QCD description.

A hard scattering QCD factorisation theorem has recently been proven for a general class of semi-inclusive processes in deep-inelastic scattering (DIS), which include the diffractive dissociation process $ep \to eXY$ [1, 2]. This implies that the concept of 'diffractive parton distributions' can be introduced, expressing proton parton probability distributions under the constraint of a leading baryonic system at a particular value of $x_{I\!P}$, integrated over a fixed range in $M_{\rm Y}$ and t. These diffractive parton distributions evolve with Q^2 according to the DGLAP equations. The phenomenology of soft hadronic interactions suggests that it may be possible to extend this factorisation to the idea of a universal pomeron exchange with parton densities dependent only on β and Q^2 and a flux factor dependent on $x_{I\!P}$ and t. Previous H1 inclusive measurements of diffractive DIS, presented in the form of a diffractive structure function $F_2^{D(3)}(\beta, Q^2, x_{I\!P})$ [3], have been found to be consistent with both collinear QCD factorisation and pomeron universality. Parton densities were extracted for the pomeron under these assumptions and were found to be dominated by a large gluon density with significant contributions at high momentum fractions β. These pomeron parton densities give a remarkably good description of measurements of the properties of hadronic final states in diffractive DIS [4], in particular jet cross sections [5], which are especially sensitive to the gluon density.

A further challenge in DIS at low x is to relate the diffractive dissociation process $ep \to eXY$ to the total cross section $ep \to eX$. Many authors (e.g. [6, 7, 8]) have attempted to do this by considering the scattering from the proton of partonic fluctuations of the photon, represented as colour dipoles.

In this paper, we present a new measurement of $F_2^{D(3)}(\beta, Q^2, x_{I\!P})$. The measurement is used to investigate the factorisation properties of diffractive DIS and to test QCD models. The new measurement represents a significant improvement in precision relative to previous HERA data [3, 9].

1.1 Kinematics of Diffractive DIS at HERA

Figure 1 illustrates the generic diffractive process at HERA of the type $ep \to eXY$. The electron (with 4-momentum k) couples to a virtual photon γ^* (q) which interacts with the proton (P). The usual DIS kinematic variables are defined as

$$Q^2 = -q^2 \; ; \qquad y = \frac{P \cdot q}{P \cdot k} \; ; \qquad x = \frac{-q^2}{2P \cdot q} \; . \tag{1}$$

The squared invariant masses of the electron-proton and photon-proton systems s and W^2 are given by

$$s = (k + P)^2 \simeq (300 \text{ GeV})^2 \; ; \qquad W^2 = (q + P)^2 \simeq ys - Q^2 \; . \tag{2}$$

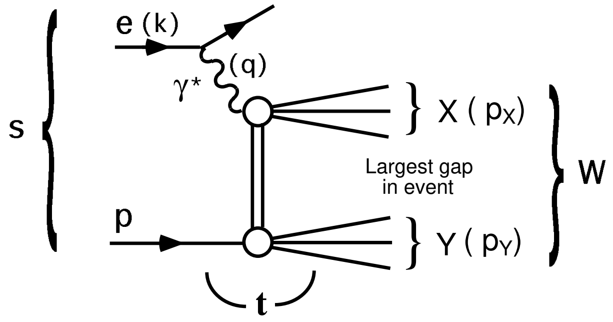

Figure 1: The generic diffractive process at HERA, where the electron (four-momentum k) couples to a photon (q) which interacts with the proton (P) via net colour singlet exchange, producing two distinct final state hadronic systems X and Y. If the masses of X and Y are small compared with W, the two systems are separated by a large gap in rapidity.

If the interaction takes place via colour singlet exchange, the photon and proton dissociate to produce distinct hadronic systems X and Y, with invariant masses M_X and M_Y respectively. In the case where M_X and M_Y are small compared with W, the two systems are separated by a large rapidity gap. The longitudinal momentum fraction $x_{I\!P}$ of the colourless exchange with respect to the incoming proton and the squared four-momentum transferred at the proton vertex t are then defined by

$$x_{I\!P} = \frac{q \cdot (P - p_Y)}{q \cdot P} = \frac{Q^2 + M_X^2 - t}{Q^2 + W^2 - M_p^2} \, ; \qquad t = (P - p_Y)^2 \, , \tag{3}$$

where p_Y is the 4-momentum of Y. In the analysis presented here, t and M_Y are not well measured. The results are thus integrated over $|t| < 1.0 \ \mathrm{GeV}^2$ and $M_{\mathrm{Y}} < 1.6 \ \mathrm{GeV}$.

In addition, the quantity β is defined as

$$\beta = \frac{x}{x_{I\!P}} = \frac{Q^2}{2q \cdot (P - p_Y)} = \frac{Q^2}{Q^2 + M_X^2 - t} \, . \tag{4}$$

In an interpretation in which partonic structure is ascribed to the colourless exchange, β is the longitudinal momentum fraction of the exchange that is carried by the struck quark, in analogy to x in the case of inclusive scattering.

2 Data and Analysis Method

A full description of the H1 apparatus can be found in [10]. The coordinate system used is such that $\theta = 0$ corresponds to the direction of the outgoing proton beam. The region of low θ and large pseudorapidity η is referred to as the 'forward' direction.

The data used for the measurement were taken during 1997, when HERA collided protons of energy $820 \ \mathrm{GeV}$ with positrons of energy $27.5 \ \mathrm{GeV}$. The measurement covers the kinematic region $Q^2 > 6\ \mathrm{GeV}^2$, $y > 0.04$ and $x_{I\!P} < 0.05$. For $Q^2 > 13.5\ \mathrm{GeV}^2$, a luminosity of $10.6\ \mathrm{pb}^{-1}$ is used in the analysis, yielding an increase in statistics relative to previous measurements [3, 9] by a factor of approximately 5. For the region $6 < Q^2 < 13.5\ \mathrm{GeV}^2$, a sample of $2.0\ \mathrm{pb}^{-1}$ is used, taken during a period when the experiment ran with dedicated triggers for low Q^2 DIS.

The data were triggered principally on the basis of an energetic cluster in the electromagnetic section of the backward 'SPACAL' calorimeter, for which the efficiency is close to 100% throughout the measured kinematic region. Events are accepted for the analysis if they contain a positron candidate with energy $E'_e > 8$ GeV in the polar angle range $156° < \theta_e < 176°$, linked to a reconstructed charged track in the backward drift chambers. A reconstructed event vertex is required from the Central Tracking Detector.

Diffractive events are selected on the basis of a large rapidity gap separating the leading baryonic system Y from the photon dissociation system X. The large rapidity gap is identified by the absence of activity in detectors sensitive to forward energy flow. The region of the main Liquid Argon Calorimeter with $\eta > 3.2$ must show no energy deposits above noise levels. There must also be no significant activity in the 'Proton Remnant Tagger' scintillators surrounding the beam at $z \sim 26$ m and sensitive to energy flow in the region $6.0 < \eta < 7.5$, the Forward Muon Detector ($5.0 < \eta < 6.5$) or the Plug calorimeter ($3.5 < \eta < 5.5$).

The mass M_{X} of the system X is measured from the hadronic activity in the SPACAL and Liquid Argon calorimeters and the tracking detectors using a method that combines tracks and calorimeter deposits without double counting. A minimum of two hadronic final state objects are required for the analysis. In order to suppress photoproduction background and ensure good reconstruction of kinematic variables, close agreement is required between y as obtained using the electron only, hadron only and double angle reconstruction methods.

The reconstruction of kinematic variables is performed using very similar techniques to those described in [3]. To reconstruct y, Q^2 and x, a mixed method is used, which reduces to the electron method at high y and the double angle method at low y.

$$y = y_e^2 + y_d\,(1 - y_d)\ ; \qquad Q^2 = \frac{4E_e^2\,(1-y)}{\tan^2(\theta_e/2)}\ ; \qquad x = Q^2/s \cdot y\ , \tag{5}$$

where y_e and y_d are the values of y as reconstructed from the electron and double angle methods respectively, E_e is the positron beam energy and θ_e is the polar angle of the scattered positron. The mass of the system X is obtained from

$$M_x^2 = (E^2 - p_x^2 - p_y^2 - p_z^2)_{\mathrm{hadrons}} \cdot \frac{y}{y_h}\ , \tag{6}$$

where y_h is the value of y reconstructed using the hadron only method. This method of M_{X} reconstruction reduces essentially to a measurement of the total $E + p_z$ of the hadrons in the limit of high y, where losses in the backward direction become significant. To account for residual losses, the measured M_{X} is scaled by 1.08. The remaining kinematic variables are reconstructed using

$$\beta = \frac{Q^2}{Q^2 + M_{\mathrm{X}}^2}\ ; \qquad x_{I\!P} = \frac{x}{\beta}\ . \tag{7}$$

Corrections for detector inefficiencies, migrations between measurement intervals and the acceptance of the selection are performed using a Monte Carlo simulation which combines several different models. The RAPGAP [11] model is used to simulate dissociative processes with $x_{\mathbb{P}} < 0.15$, arising from pomeron and sub-leading meson exchange. The DIFFVM model [12] is used to simulate the quasi elastic production of the ρ, ω, ϕ and J/ψ vector mesons. Smearing from the region $x_{\mathbb{P}} > 0.15$ is modelled using the DJANGO [13] Monte Carlo model. The small QED-Compton background at the largest β is subtracted using the COMPTON [14] Monte Carlo model. Photoproduction background, which is negligible except at the highest y values, is subtracted using the PHOJET [15] model. Figure 2 shows comparisons between the uncorrected data and the full Monte Carlo simulation for several important variables used in the reconstruction. The simulation gives a good overall description of the data.

The large rapidity gap selection yields a sample dominated by the single dissociation process $ep \rightarrow eXp$, with a small admixture of double dissociation events of the type $ep \rightarrow eXY$ where the proton dissociation system has a small mass M_{Y}. The measurement is corrected to the region $M_{\mathrm{Y}} < 1.6$ GeV and $t > -1$ GeV^2 as was the case for previous H1 data [3]. The final structure functions correspond to the case where the systems X and Y are separated by the largest gap in the rapidity distribution of the final state hadrons. The correction factor applied to account for smearing about the M_{Y} and t boundaries of the measurement is $-8.7 \pm 8.2\%$.

3 Structure Function Extraction

Two different binning schemes are used in the measurement. In the first, the differential cross section $\mathrm{d}^3\sigma/(\mathrm{d}\beta\ \mathrm{d}Q^2\ \mathrm{d}x)$ is measured at a large number of x values, to allow detailed investigation of the $x_{\mathbb{P}}$ (or $x = x_{\mathbb{P}} \cdot \beta$) dependence of the data. The structure function is then extracted using

$$F_2^{D(3)}(\beta, Q^2, x_{\mathbb{P}}) = \frac{\beta^2\ Q^4}{4\pi\alpha^2\ (1 - y + y^2/2)}\ \frac{\mathrm{d}^3\sigma_{ep\rightarrow eXY}}{\mathrm{d}\beta\ \mathrm{d}Q^2\ \mathrm{d}x}\ , \tag{8}$$

where α is the fine structure constant. In the second binning scheme, the differential cross section $\mathrm{d}^3\sigma/(\mathrm{d}\beta\ \mathrm{d}Q^2\ \mathrm{d}x_{\mathbb{P}})$ is extracted at four fixed values of $x_{\mathbb{P}}$. This second method allows the β and Q^2 dependence of the data and its variation with $x_{\mathbb{P}}$ to be studied with high precision. The structure function is extracted using

$$F_2^{D(3)}(\beta, Q^2, x_{\mathbb{P}}) = \frac{\beta\ Q^4}{4\pi\alpha^2\ (1 - y + y^2/2)}\ \frac{\mathrm{d}^3\sigma_{ep\rightarrow eXY}}{\mathrm{d}\beta\ \mathrm{d}Q^2\ \mathrm{d}x_{\mathbb{P}}}\ . \tag{9}$$

For both schemes, $F_2^{D(3)}$ is extracted under the assumption that the longitudinal structure function $F_L^{D(3)} = 0$. This assumption has negligible influence on the extracted $F_2^{D(3)}$, except at the largest y values, corresponding to the lowest $x_{\mathbb{P}}$. The effect of a non-zero value of $F_L^{D(3)}$ is discussed in section 4.1.

For all data points shown, the total acceptance exceeds 40%, the acceptance of the forward detector selection is greater than 50% and the bin purities exceed 30%. Corrections for initial and final state electromagnetic radiation and QED virtual loops are performed using the RAPGAP Monte Carlo model via an interface to HERACLES [16]. The final measurements are quoted at the Born level.

A detailed systematic error analysis has been performed in which the sensitivity of the measurement to variations in the efficiencies and energy scales of the detector components and to variations in the details of the Monte Carlo models used for corrections are evaluated. The resulting systematic error is in the range 10-15% for most of the data points, the largest contribution arising from the correction to the measured $M_{\rm Y}$ and t regions in most cases.

4 Results

The measured $F_2^{D(3)}$ is compared with previous H1 data [3] in figure 3. The improved statistics of the new measurement allow the structure function to be extracted in an increased number of Q^2 and $x_{I\!P}$ bins. In the region $Q^2 > 15~\mathrm{GeV}^2$, the statistical precision is considerably improved. The two measurements are in good agreement with the exception of the low β, medium Q^2 (large $M_{\rm X}$) region, where the previous data tend to be slightly higher than the new measurement.

4.1 The $x_{I\!P}$ dependence of F_2^D

The $x_{I\!P}$ dependence of the measured diffractive structure function $F_2^{D(3)}(\beta, Q^2, x_{I\!P})$ for fixed β and Q^2 is studied, following a similar procedure to that adopted in [3]. A fit is performed to the data using a parameterization of the form

$$F_2^D(x_{I\!P}, \beta, Q^2) = f_{I\!P}(x_{I\!P}) A_{I\!P}(\beta, Q^2) + f_{I\!R}(x_{I\!P}) B_{I\!R}(\beta, Q^2) \,, \tag{10}$$

which is motivated by the ideas of Regge phenomenology. $f_{I\!P}(x_{I\!P})$ and $f_{I\!R}(x_{I\!P})$ correspond to pomeron and sub-leading reggeon *flux factors* and are defined as

$$f_{\{I\!P,I\!R\}}(x_{I\!P}) = \int_{t_{cut}}^{t_{min}} \frac{e^{B_{\{I\!P,I\!R\}} t}}{x_{I\!P}^{2\alpha_{\{I\!P,I\!R\}}(t)-1}} \, \mathrm{d}t \,, \tag{11}$$

where $t_{cut} = -1.0~\mathrm{GeV}^2$, $|t_{min}|$ is the minimum kinematically allowed value of $|t|$ and the pomeron and reggeon trajectories are assumed to be linear:

$$\alpha_{\{I\!P,I\!R\}}(t) = \alpha_{\{I\!P,I\!R\}}(0) + \alpha'_{\{I\!P,I\!R\}} t \,. \tag{12}$$

The values for $\alpha'_{I\!P}$, $B_{I\!P}$, $\alpha'_{I\!R}$ and $B_{I\!R}$ cannot be constrained by the $F_2^{D(3)}$ data and are taken from other measurements. Furthermore, the secondary reggeon trajectory intercept $\alpha_{I\!R}(0)$ is not well constrained by the data due to a lack of high precision data points at high $x_{I\!P}$ (low y) values. It is taken from a similar fit to previous H1 $F_2^{D(3)}$ data as described in [3]. The values assumed for the parameterization of the pomeron and reggeon flux factors are $\alpha'_{I\!P} = 0.26 \pm 0.26~\mathrm{GeV}^{-2}$, $B_{I\!P} = 4.6^{+3.4}_{-2.6}~\mathrm{GeV}^{-2}$, $\alpha'_{I\!R} = 0.90 \pm 0.10~\mathrm{GeV}^{-2}$, $B_{I\!R} = 2.0 \pm 2.0~\mathrm{GeV}^{-2}$ and $\alpha_{I\!R}(0) = 0.50 \pm 0.16$. The longitudinal structure function F_L^D is assumed to be zero.

A fit is performed to all data with $y < 0.45$ in every (Q^2,β) bin of the measurement which contains at least four data points. The cut in y limits the influence of a non-zero value of F_L^D. In the fit, the value for the pomeron intercept parameter $\alpha_{I\!P}(0)$ is left as a free parameter, as are the coefficients $A_{I\!P}(\beta, Q^2)$ and $B_{I\!R}(\beta, Q^2)$ in each (Q^2,β) bin. The fit gives a very good description of the data ($\chi^2/\mathrm{ndf} = 0.95$). If the presence of a sub-leading reggeon exchange contribution is neglected in the fit, the description of the data is considerably poorer and a significantly worse $\chi^2/\mathrm{ndf} = 1.25$ is obtained. The systematic error on $\alpha_{I\!P}(0)$ is obtained by repeating the fit after shifting the data points according to each individual source of systematic uncertainty.

The possibility of interference between the pomeron and reggeon exchange contributions is taken into account by repeating the fit with the assumption of maximum interference, where the interference flux is parameterized according to eqs. (14,16) in [3]. Since no significant change in χ^2 is observed with or without interference, the results quoted for the values of $\alpha_{I\!P}(0)$ correspond to the averages of the values obtained with or without interference and their difference is included in the uncertainty on $\alpha_{I\!P}(0)$.

Further model dependences of the extracted value of $\alpha_{I\!P}(0)$ are estimated by varying the assumed values for $\alpha'_{I\!P}$, $B_{I\!P}$, $\alpha'_{I\!R}$, $B_{I\!R}$ and $\alpha_{I\!R}(0)$ within the limits quoted above. The lack of knowledge on the size of F_L^D is taken into account by repeating the fit under the extreme assumption of $F_L^{D(3)} = F_2^{D(3)}$ and taking the difference in the result as an additional model dependence uncertainty.

The result of the fit is

$$\alpha_{I\!P}(0) = 1.173 \ \pm 0.018 \ (\mathrm{stat.}) \ \pm 0.017 \ (\mathrm{syst.}) \ ^{+0.063}_{-0.035} \ (\mathrm{model}) \, . \tag{13}$$

The dominant contribution to the model dependence error on $\alpha_{I\!P}(0)$ originates from the unknown value of $F_L^{D(3)}$. The fit result is illustrated in figure 4. The obtained value for the pomeron intercept is significantly higher than the value $\alpha_{I\!P}(0) \simeq 1.08$ for the *soft pomeron* [17] describing soft hadronic interactions. The result is compatible with that obtained from similar fits to previous H1 $F_2^{D(3)}$ data [3].

Two further fits are performed in order to investigate whether $\alpha_{I\!P}(0)$ has any dependence on Q^2. The data are divided into two Q^2 intervals covering the data with $6.5 < Q^2 < 20 \ \mathrm{GeV}^2$ and $25 < Q^2 < 120 \ \mathrm{GeV}^2$ respectively. The results are

$$\alpha_{I\!P}(0) = 1.162 \ \pm 0.021 \ (\mathrm{stat.}) \ \pm 0.018 \ (\mathrm{syst.}) \ ^{+0.064}_{-0.034} \ (\mathrm{model}) \quad (\langle Q^2 \rangle = 10.8 \ \mathrm{GeV}^2) \tag{14}$$

and

$$\alpha_{I\!P}(0) = 1.204 \ \pm 0.034 \ (\mathrm{stat.}) \ \pm 0.027 \ (\mathrm{syst.}) \ ^{+0.060}_{-0.037} \ (\mathrm{model}) \quad (\langle Q^2 \rangle = 49.5 \ \mathrm{GeV}^2) \, . \tag{15}$$

These results are shown together with the previous H1 measurement in figure 5. Within the uncertainties, there is no evidence for a variation of $\alpha_{I\!P}(0)$ with Q^2 in the measured kinematic range. In figure 5, the effective pomeron intercept extracted from the diffractive data is compared with $\alpha_{I\!P}(0) = \lambda + 1$ as obtained from fits of the form $F_2 = cx^{-\lambda(Q^2)}$ to inclusive small x proton structure function data [18]. The data suggest that at large Q^2, the effective intercept describing the inclusive data is larger than that from the diffractive data.

4.2 The Ratio F_2^D/F_2

The $\gamma^* p$ centre of mass energy dependences of the diffractive and inclusive cross sections are further compared in figure 6. Here, the quantity

$$\rho^{D(3)}(\beta, Q^2, x) \;=\; \frac{M_{\rm X}^2\;x}{Q^2}\;\cdot\;\frac{F_2^{D(3)}(\beta, Q^2, x_{I\!P})}{F_2(x, Q^2)} \tag{16}$$

is plotted as a function of W in bins of fixed Q^2 and β. The F_2 data are taken from [18]. In order to improve the statistical precision, measurements at adjacent Q^2 values have been combined. In terms of virtual photon-proton cross sections,

$$\rho^{D(3)} \;=\; M_{\rm X}^2\,\frac{{\rm d}\sigma(\gamma^* p \to XY)}{{\rm d}M_{\rm X}^2}\;\;/\;\;\sigma(\gamma^* p \to X)\,, \tag{17}$$

where the diffractive cross section is integrated over $M_{\rm Y} < 1.6$ GeV and $|t| < 1\ {\rm GeV}^2$. Up to a factor of $M_{\rm X}^2/(Q^2 + M_{\rm X}^2)$, $\rho^{D(3)}$ is equal to the quantity $r^{D(3)}$ constructed from previous H1 data [19]. The ratio $\rho^{D(3)}$ is relatively flat throughout the full phase space, except at large β values (the very low $M_{\rm X}$ region) and at low W, where sub-leading exchanges play a role in the diffractive data. The relative flatness of the data is consistent with the observation by ZEUS in [9].

4.3 The β and Q^2 Dependences of $F_2^{D(3)}$

Figures 7 and 8 show the β dependence of the data at different Q^2 values at fixed values of $x_{I\!P} = 0.001$, 0.003, 0.01 and 0.03. Figures 9 and 10 show the Q^2 dependence at different β values for the same four fixed values of $x_{I\!P}$. In figure 10, preliminary H1 data at larger Q^2 [20] are also included.

The data show similar properties to previous $F_2^{D(3)}$ measurements, but with much improved precision. The β dependence is relatively flat, with large contributions at high fractional momenta, in contrast to hadronic structure functions. The data exhibit rising scaling violations up to values of β at least as large as 0.4, falling with Q^2 only at the highest value $\beta = 0.9$. The β dependence at fixed $x_{I\!P}$ thus evolves from high to low β with increasing Q^2, as expected for DGLAP evolution dominated by gluon radiation.

The data in figures 7–10 are compared with the results of a fit to the data in which the β and Q^2 dependences evolve according to the DGLAP equations and the $x_{I\!P}$ dependence follows a Regge behaviour with pomeron ($I\!P$) and sub-leading meson ($I\!R$) exchange contributions, the flux factors being as described in section 4.1. In the fit, light singlet quark (u, d, s) and gluon distributions are considered, parameterised in terms of non-perturbative input distributions at the starting scale $Q_0^2 = 2\ {\rm GeV}^2$ for the QCD evolution. Only data with $y < 0.45$, $\beta \leq 0.65$ and $M_X > 2$ GeV are included in the fit. The fit gives a very good description of the data, including the kinematic region that was not included in the fit. The resulting parton distributions are dominated by a large gluon distribution extending to large β at low scales. Sub-leading exchange contributions are negligible for $x_{I\!P} \leq 0.003$ and become significant only at large $x_{I\!P}$ and low β.

In figures 11 and 12, the Q^2 dependence of the data at fixed $x_{I\!P}$ and β (and hence fixed x) is compared with the Q^2 dependence of $F_2(x, Q^2)$ data from [18] at the same values of x. In the region of low β, the scaling violations of $F_2^{D(3)}$ are similar to those of F_2 at the same value of x. However, at the largest values $\beta = 0.9$, $F_2^{D(3)}$ falls with increasing Q^2, whereas F_2 continues to rise.

4.4 Comparisons with Models

In figure 13, the Q^2 and β dependences of the measured $F_2^{D(3)}(\beta, Q^2, x_{I\!P})$ at fixed $x_{I\!P} = 0.003$ are compared with the "semi-classical" model by Buchmüller, Gehrmann and Hebecker [6]. In this model, DIS is considered in terms of the scattering from the proton of $q\bar{q}$ and $q\bar{q}g$ fluctuations of the virtual photon, modelled as colour dipoles. The partonic fluctuations of the photon scatter from a superposition of colour fields of the proton according to a simple non-perturbative model that averages over all colour field configurations. All resulting final state configurations contribute to the inclusive proton structure function $F_2(x, Q^2)$. Those in which the scattered partons emerge in a net colour-singlet state contribute to the diffractive structure function F_2^D. The model contains only four free parameters, which are obtained from a combined fit to previous F_2 and F_2^D data. The model reproduces the general features of the data but lies above the data where β and Q^2 are both small. The behaviour of F_2^D in the region of small masses $M_X^2 < 4\ \mathrm{GeV}^2$ (corresponding to large β), is not expected to be reproduced by the model.

The data are compared in figure 14 with two versions of another colour dipole model by Golec-Biernat and Wüsthoff [7, 8]. In this model, the $q\bar{q}$ and $q\bar{q}g$ dipole cross sections are obtained from fits to F_2 data. The same dipole cross sections are then used to predict $F_2^{D(3)}(\beta, Q^2, x_{I\!P})$ under the assumption of two-gluon exchange, with only one additional free parameter, corresponding to the exponential t dependence of the data, e^{Bt} where $B = 6\ \mathrm{GeV}^{-2}$. Unlike the semi-classical model, the saturation model also contains a higher twist contribution at large β, allowing comparisons to be made throughout the full measured kinematic region. The model in [7] gives a good description of the data except at small β and Q^2. The model in [8], in which QCD evolution is added, underestimates the measured $F_2^{D(3)}(\beta, Q^2, x_{I\!P})$ at high β and high Q^2.

The $x_{I\!P}$ dependence of the measured $F_2^{D(3)}(\beta, Q^2, x_{I\!P})$ at fixed β and Q^2 is compared with two versions of the "Soft Colour Interactions" (SCI) model [21, 22] in figure 15. In these models, the hard interaction in diffractive DIS is treated identically to that in inclusive DIS. Diffraction occurs through soft colour rearrangements between the outgoing partons, leaving their momentum configuration unchanged. In the original SCI model [21], diffractive final states are produced using only one free parameter, the universal colour rearrangement probability, which is fixed by a fit to $F_2^{D(3)}$. The model has been refined recently [22] by making the colour rearrangement probability proportional to the normalised difference in the generalised areas of the string configurations before and after the rearrangement. The kinematic region shown in figure 15 is restricted to $M_X > 2\ \mathrm{GeV}$, corresponding to the region for which the model is intended. The model predictions have been obtained using the LEPTO $6.5.2\beta$ [23] Monte Carlo generator. The improved version of SCI based on a generalized area law [22] results in a better description of $F_2^{D(3)}(\beta, Q^2, x_{I\!P})$ at low Q^2 than the original version in [21], with the exception of the highest β region.

5 Conclusions

A new measurement of the diffractive structure function $F_2^{D(3)}(\beta, Q^2, x_{I\!P})$ has been presented for $6.5 < Q^2 < 120\ \mathrm{GeV}^2$, $0.01 < \beta < 0.9$ and $x_{I\!P} < 0.05$. In the region $Q^2 \geq 15\ \mathrm{GeV}^2$, the measurement is significantly more precise than previous data.

The $x_{I\!P}$ dependence of the data is well described by a model motivated by Regge phenomenology, in which a leading ($I\!P$) and a secondary ($I\!R$) exchange contribute. The effective pomeron intercept describing the data is

$$\alpha_{I\!P}(0) = 1.173\ \pm 0.018\ (\mathrm{stat.})\ \pm 0.017\ (\mathrm{syst.})\ ^{+0.063}_{-0.035}\ (\mathrm{model})\ .$$

The results suggest that the effective pomeron intercepts describing the total and the diffractive dissociation cross sections for $\gamma^* p$ interactions become different at large Q^2. The ratio of the t-integrated diffractive to the total $\gamma^* p$ cross section is relatively flat as a function of $\gamma^* p$ centre of mass energy.

At fixed $x_{I\!P}$ the data show a relatively flat β dependence and a rising dependence on Q^2, except at the highest values of β. This structure is well described by a fit based on DGLAP evolution of the β and Q^2 dependence and a Regge motivated $x_{I\!P}$ dependence. In this fit, the diffractive parton distributions of the proton are heavily dominated by a large gluon density. The scaling violations of F_2^D are similar to those of F_2 when compared at the same x values, except at large β where vector meson and other higher twist contributions are expected to play a significant role in the diffractive data.

Acknowledgements

We are grateful to the HERA machine group whose outstanding efforts have made and continue to make this experiment possible. We thank the engineers and technicians for their work in constructing and now maintaining the H1 detector, our funding agencies for financial support, the DESY technical staff for continual assistance, and the DESY directorate for the hospitality which they extend to the non DESY members of the collaboration.

References

[1] L. Trentadue, G. Veneziano, *Phys. Lett.* **B 323** (1994) 201;
A. Berera, D. Soper, *Phys. Rev.* **D 50** (1994) 4328;
M. Grazzini, L. Trentadue, G. Veneziano, *Nucl. Phys.* **B 519** (1998) 394.

[2] J. Collins, *Phys. Rev.* **D 57** (1998) 3051 and erratum-ibid. **D 61** (2000) 019902.

[3] H1 Collaboration, C. Adloff *et al.*, *Z. Phys.* **C 76** (1997) 613.

[4] H1 Collaboration, C. Adloff *et al.*, *Eur. Phys. J.* **C 1** (1998) 495;
H1 Collaboration, C. Adloff *et al.*, *Phys. Lett.* **B 428** (1998) 206;
H1 Collaboration, C. Adloff *et al.*, *Eur. Phys. J.* **C 5** (1998) 439.

[5] H1 Collaboration, C. Adloff *et al.*, *Eur. Phys. J.* **C 20** (2001) 29;
H1 Collaboration, C. Adloff *et al.*, *Eur. Phys. J.* **C 6** (1999) 421.

[6] W. Buchmüller, T. Gehrmann, A. Hebecker, *Nucl. Phys.* **B 537** (1999) 477.

[7] K. Golec-Biernat, M. Wüsthoff, *Phys. Rev.* **D 59** (1999) 014017;
K. Golec-Biernat, M. Wüsthoff, *Phys. Rev.* **D 60** (1999) 114023.

[8] K. Golec-Biernat, M. Wüsthoff, *Eur. Phys. J.* **C 20** (2001) 313.

[9] ZEUS Collaboration, J. Breitweg *et al.*, *Eur. Phys. J.* **C 6** (1999) 43.

[10] H1 Collaboration, I. Abt *et al.*, *Nucl. Instrum. Methods* **A 386** (1997) 310 and 348.

[11] H. Jung, *Comp. Phys. Commun.* **86** (1995) 147.
(see also http://www.desy.de/∼jung/rapgap.html)

[12] B. List: *Diffraktive J/ψ-Produktion in Elektron-Proton-Stößen am Speicherring HERA*, Diploma Thesis, Tech. Univ. Berlin (1993), unpublished;
B. List, A. Mastroberardino: *DIFFVM: A Monte Carlo Generator for diffractive processes in ep scattering* in *Monte Carlo Generators for HERA Physics*, A. Doyle, G. Grindhammer, G. Ingelman, H. Jung (eds.), DESY-PROC-1999-02 (1999) 396.

[13] G. Schuler and H. Spiesberger, Proc. of the Workshop on Physics at HERA, Vol. 3, eds. W. Buchmüller and G. Ingelman, Hamburg, DESY (1992), p. 1419.

[14] A. Courau *et al.*, Proc. of the Workshop on Physics at HERA, Vol. 2, eds. W. Buchmüller and G. Ingelman, Hamburg, DESY (1992), p. 902.

[15] R. Engel and J. Ranft, Phys. Rev. D **54** (1996) 4244.

[16] A. Kwiatkowski, H. Spiesberger, H. Möhring, *Comp. Phys. Commun.* **69** (1992) 155.

[17] A. Donnachie, P. Landshoff, *Phys. Lett.* **B 296** (1992) 227;
J. Cudell, K. Kang, S. Kim, *Phys. Lett.* **B 395** (1997) 311.

[18] H1 Collaboration, C. Adloff *et al.*, *Deep-Inelastic Inclusive ep Scattering at Low x and a Determination of α_s*, hep-ex/0012053, acc. by *Eur. Phys. J.* **C**.

[19] A. Mehta, *Comparison of Diffractive and Non-Diffractive Deep Inelastic Scattering*, Proceedings of the 10th Workshop on Photon-Photon Collisions, Sheffield, UK, April 1995.

[20] H1 Collaboration, *Measurement and Interpretation of the Diffractive Structure Function $F_2^{D(3)}$ at HERA*, Paper 571, ICHEP98, Vancouver, Canada (1998).

[21] A. Edin, G. Ingelman, J. Rathsman, *Phys. Lett.* **B 366** (1996) 371;
A. Edin, G. Ingelman, J. Rathsman, *Z. Phys.* **C 75** (1997) 57.

[22] J. Rathsman, *Phys. Lett.* **B 452** (1999) 364.

[23] A. Edin, G. Ingelman, J. Rathsman, *Comp. Phys. Commun.* **101** (1997) 108.

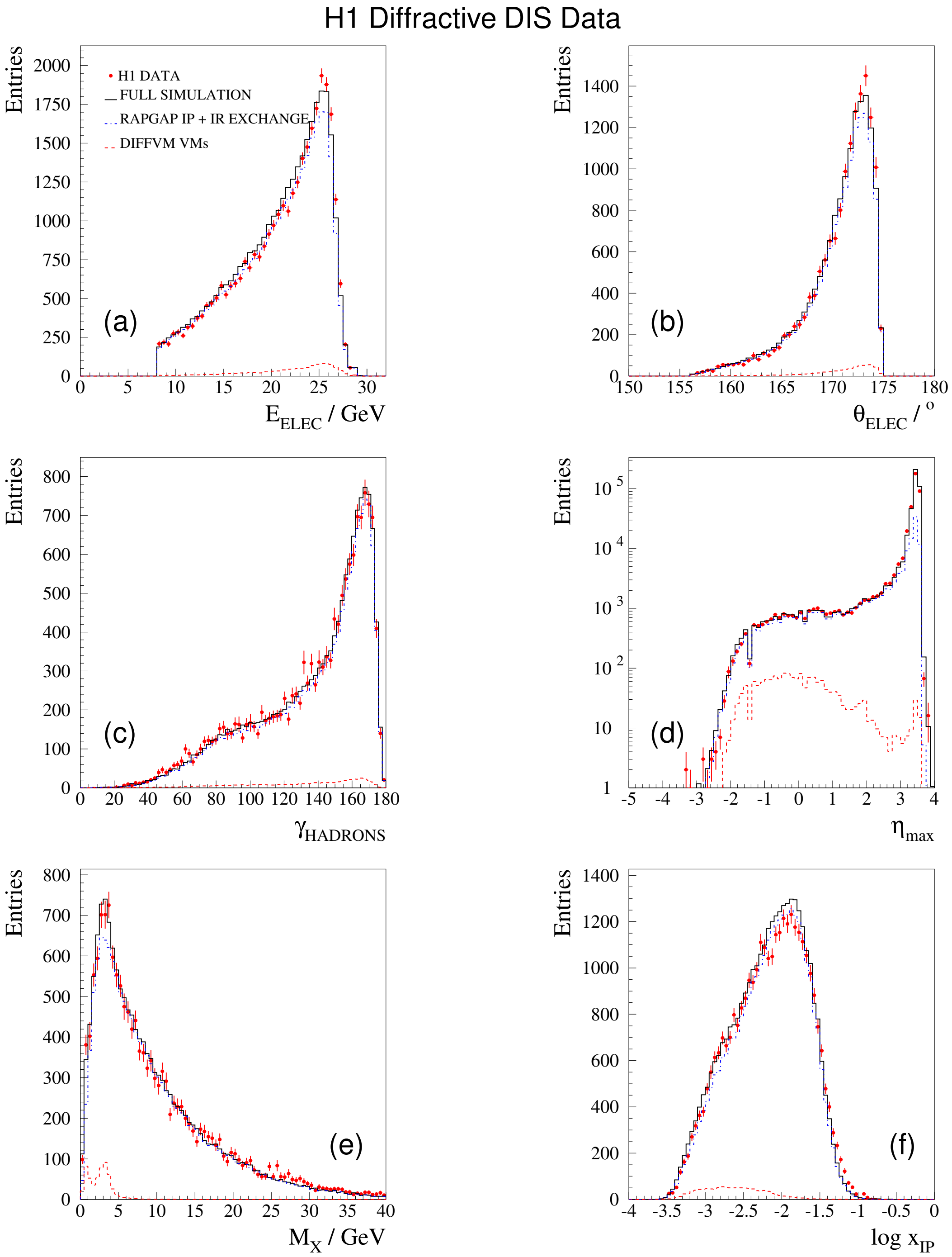

Figure 2: Observed distributions for *(a)* the scattered electron energy and *(b)* its polar angle, *(c)* the polar angle of the hadronic final state, *(d)* the maximum pseudorapidity $\eta_{\max}$ of all hadronic final state objects visible in the detector, *(e)* the invariant mass of the X system and *(f)* $x_{I\!P}$, the longitudinal momentum fraction of the proton which is transferred to the X system. The solid curves correspond to the sum of all Monte Carlo simulation contributions as described in the text, the dot-dashed curves indicate the sum of the pomeron and reggeon exchange contributions as implemented in RAPGAP and the dashed curves correspond to the contributions from vector meson production as simulated by DIFFVM.

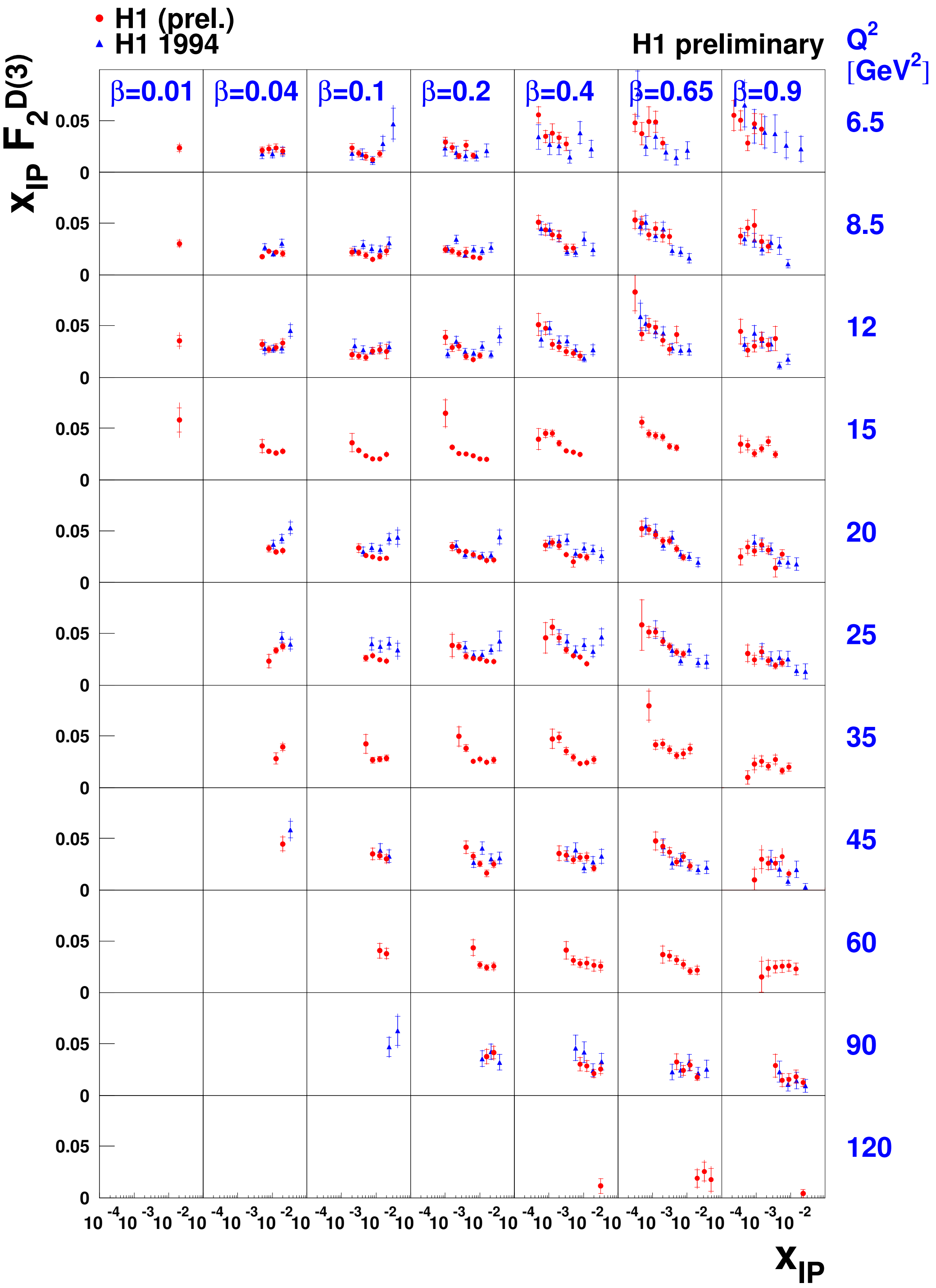

Figure 3: The measured diffractive structure function *(red filled circles)*, presented as $x_{I\!P} F_2^{D(3)}(\beta, Q^2, x_{I\!P})$ and plotted as a function of $x_{I\!P}$ at fixed values of β and Q^2. Here and in all other figures, the inner error bars correspond to the statistical error, the outer error bars show the statistical and the systematic error added in quadrature. An additional normalization uncertainty of 6.8% is not shown. For comparison, the previous H1 measurement of $F_2^{D(3)}$ in [3] is also shown *(blue triangles)*.

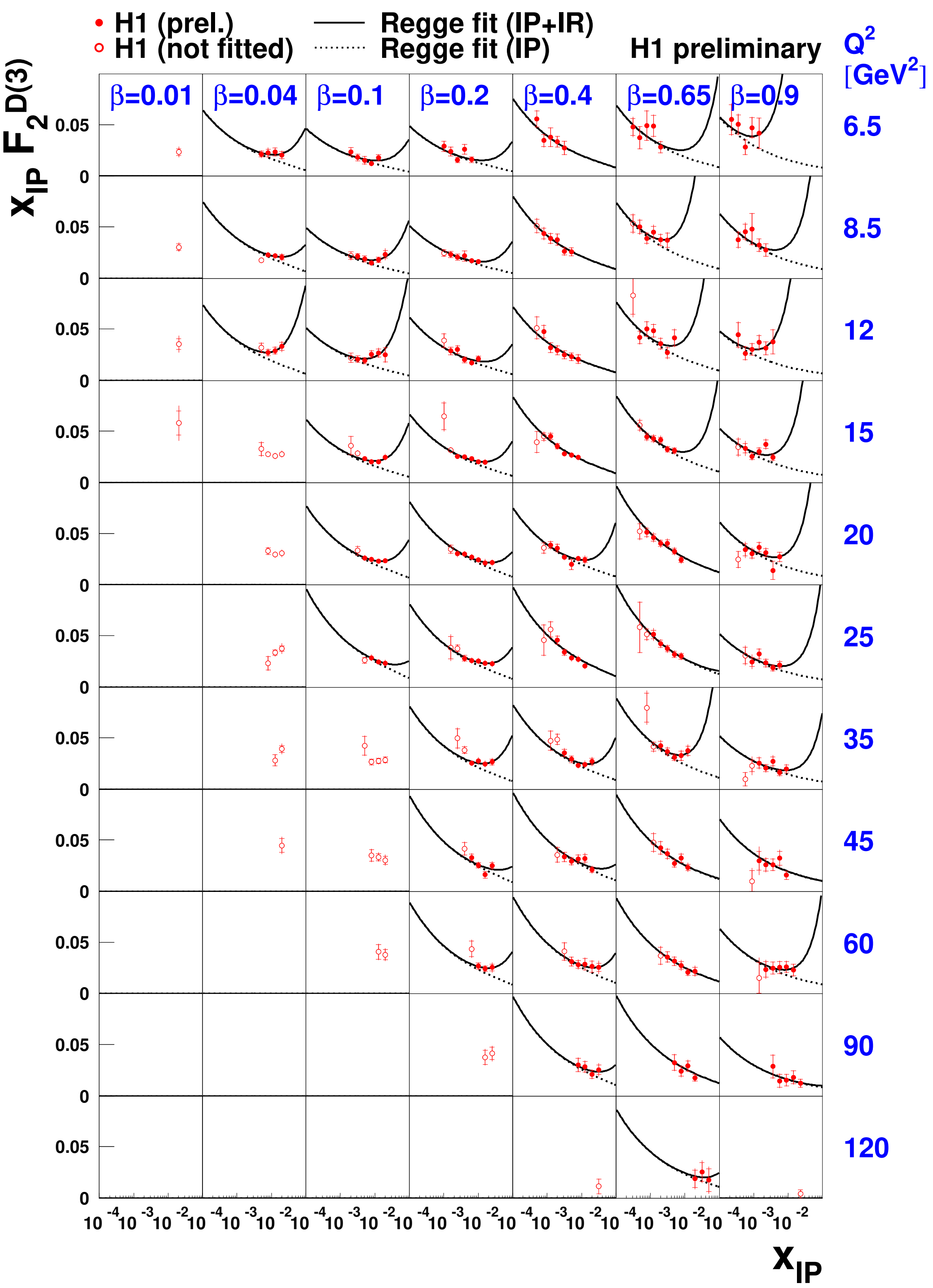

Figure 4: The measured diffractive structure function *(red filled circles)*, presented as $x_{IP} F_2^{D(3)}(\beta, Q^2, x_{IP})$ and plotted as a function of x_{IP}, at fixed values of β and Q^2. The result of the phenomenological Regge fit to the data as described in the text is shown by the curves, where the solid curve corresponds to the sum of pomeron and reggeon exchange contributions and the dotted curve indicates the contribution from pomeron exchange only. Data points which were excluded from the fit ($y > 0.45$ or $N^{\rm points}_{(\beta,Q^2)-\rm bin} < 4$) are indicated by open circles.

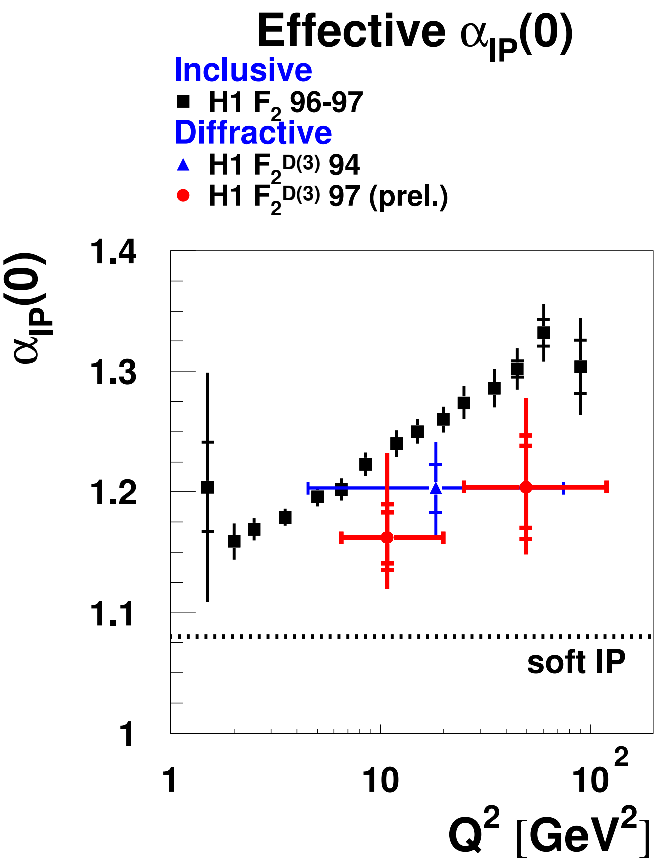

Figure 5: The effective value of $\alpha_{I\!P}(0)$ as a function of Q^2. The squares correspond to $\alpha_{I\!P}(0) = 1 + \lambda$ extracted from a fit $F_2 = cx^{-\lambda(Q^2)}$ to inclusive $F_2(x, Q^2)$ data [18] for $x < 0.01$. The red filled circles are the values of $\alpha_{I\!P}(0)$ as obtained from the phenomenological Regge fit to the F_2^D data as described in the text, for two different Q^2 intervals. The inner error bars correspond to the statistical errors. The middle error bars show the statistical and experimental systematic errors added in quadrature. The outer error bars show the full error, including that arising from model dependence. The blue triangle is the value of $\alpha_{I\!P}(0)$ which was obtained in [3].

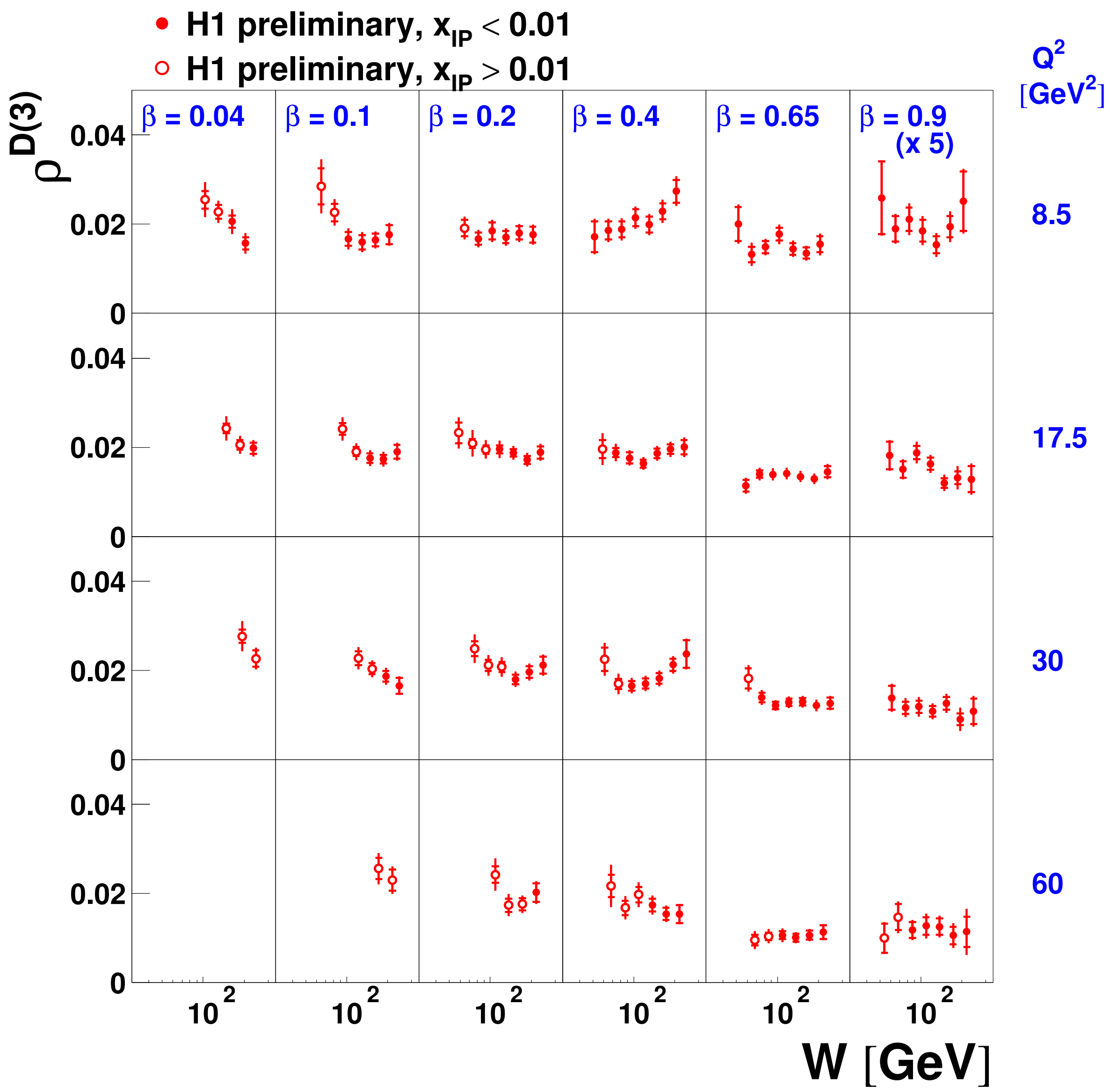

Figure 6: Measurements of $\rho^{D(3)}$, illustrating the ratio of the diffractive to the inclusive cross section. The data points at $\beta = 0.9$ have been scaled by a factor of 5 for visibility. The filled points correspond to the region $x_{\mathbb{P}} < 0.01$ in the diffractive measurement. The open points correspond to $x_{\mathbb{P}} > 0.01$. At each β and Q^2 point, the photon dissociation mass is also fixed according to $M_X^2 = Q^2\,(1/\beta - 1)$.

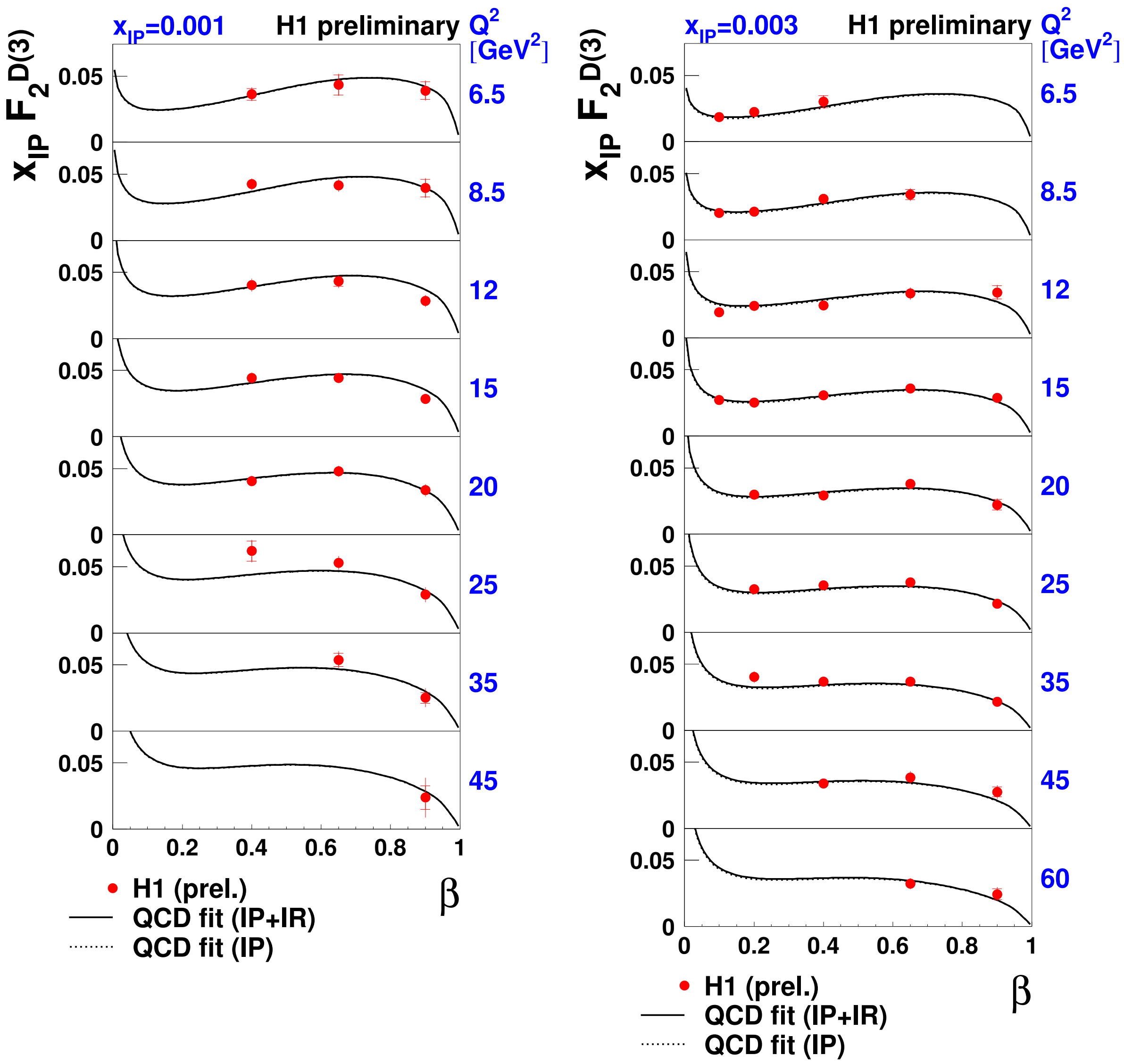

Figure 7: The measured diffractive structure function, plotted as $x_{I\!P}F_2^{D(3)}(\beta, Q^2, x_{I\!P})$ *(red data points)*, as a function of β for various values of Q^2 and at two fixed values of $x_{I\!P} = 0.001$ *(left)* and $x_{I\!P} = 0.003$ *(right)*. Also shown is the result of a QCD fit to the data as described in the text. The solid curves correspond to the sum of pomeron and sub-leading reggeon exchange contributions, whereas the dotted curves indicate the contribution from pomeron exchange only.

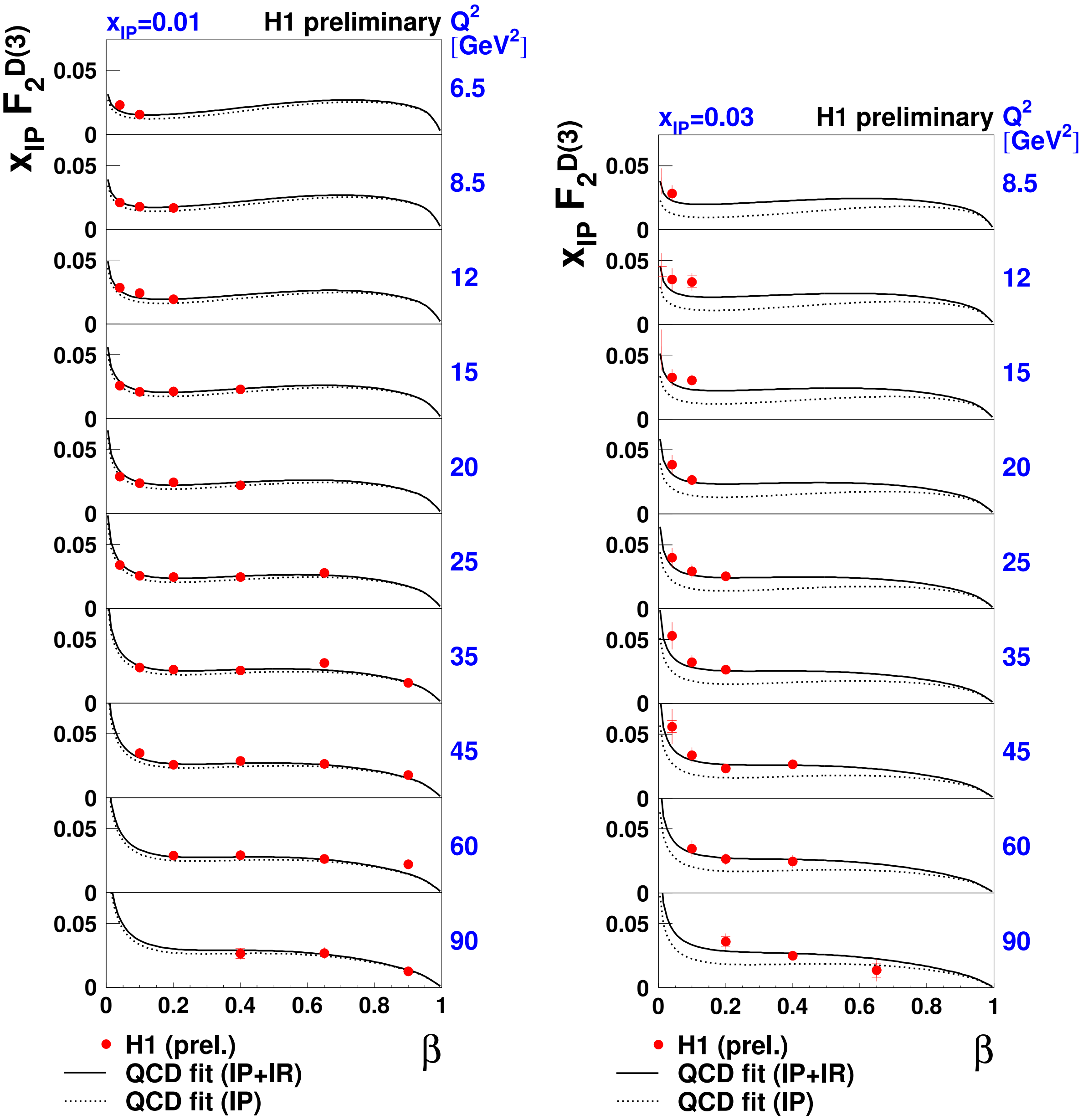

Figure 8: The measured diffractive structure function, plotted as $x_{I\!P} F_2^{D(3)}(\beta, Q^2, x_{I\!P})$ *(red data points)*, as a function of β for various values of Q^2 and at two fixed values of $x_{I\!P} = 0.01$ *(left)* and $x_{I\!P} = 0.03$ *(right)*. Also shown is the result of a QCD fit to the data as described in the text. The solid curves correspond to the sum of pomeron and sub-leading reggeon exchange contributions, whereas the dotted curves indicate the contribution from pomeron exchange only.

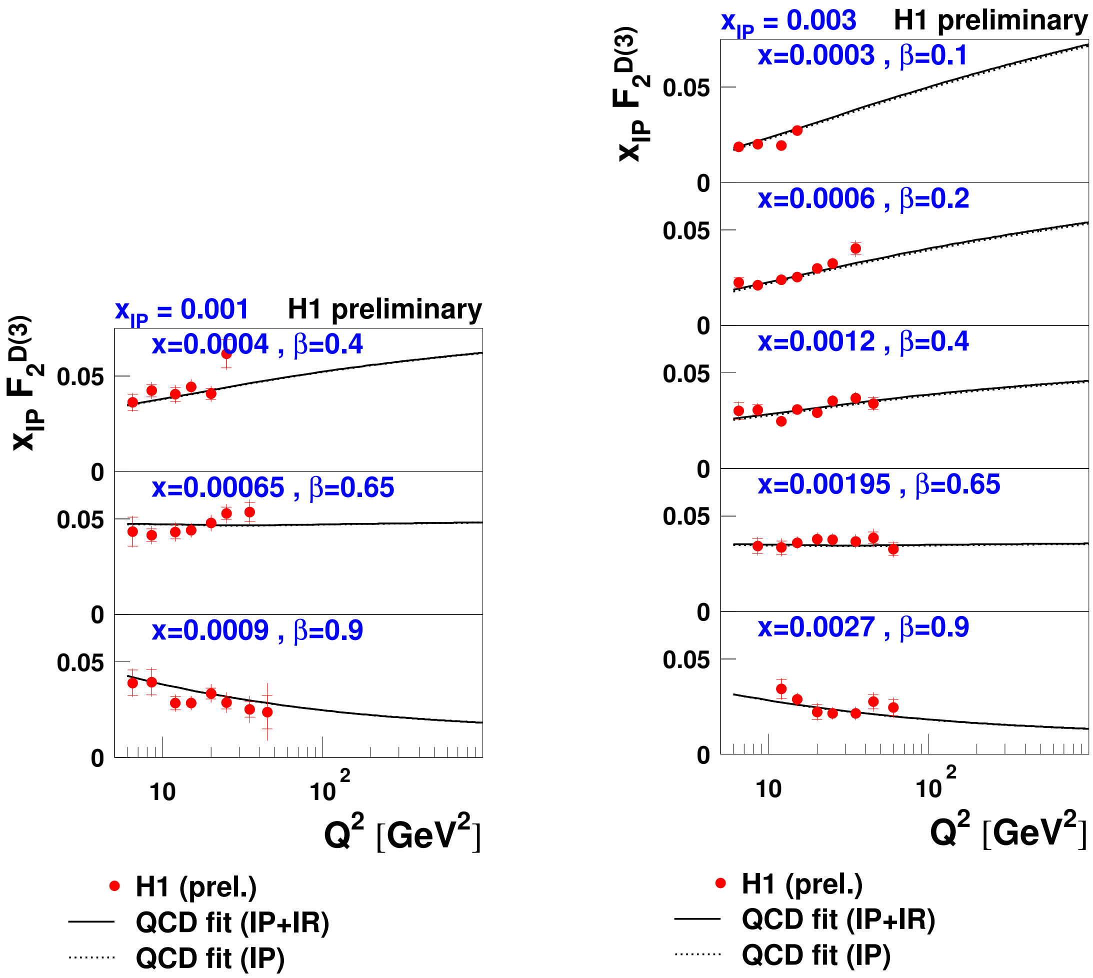

Figure 9: The measured diffractive structure function, plotted as $x_{I\!P} F_2^{D(3)}(\beta, Q^2, x_{I\!P})$ *(red data points)*, as a function of Q^2 for various values of β and at two fixed values of $x_{I\!P} = 0.001$ *(left)* and $x_{I\!P} = 0.003$ *(right)*. Also shown is the result of a QCD fit to the data as described in the text. The solid curves correspond to the sum of pomeron and sub-leading reggeon exchange contributions, whereas the dotted curves indicate the contribution from pomeron exchange only. For each value of β, the corresponding value of $x = x_{I\!P}\beta$ is indicated.

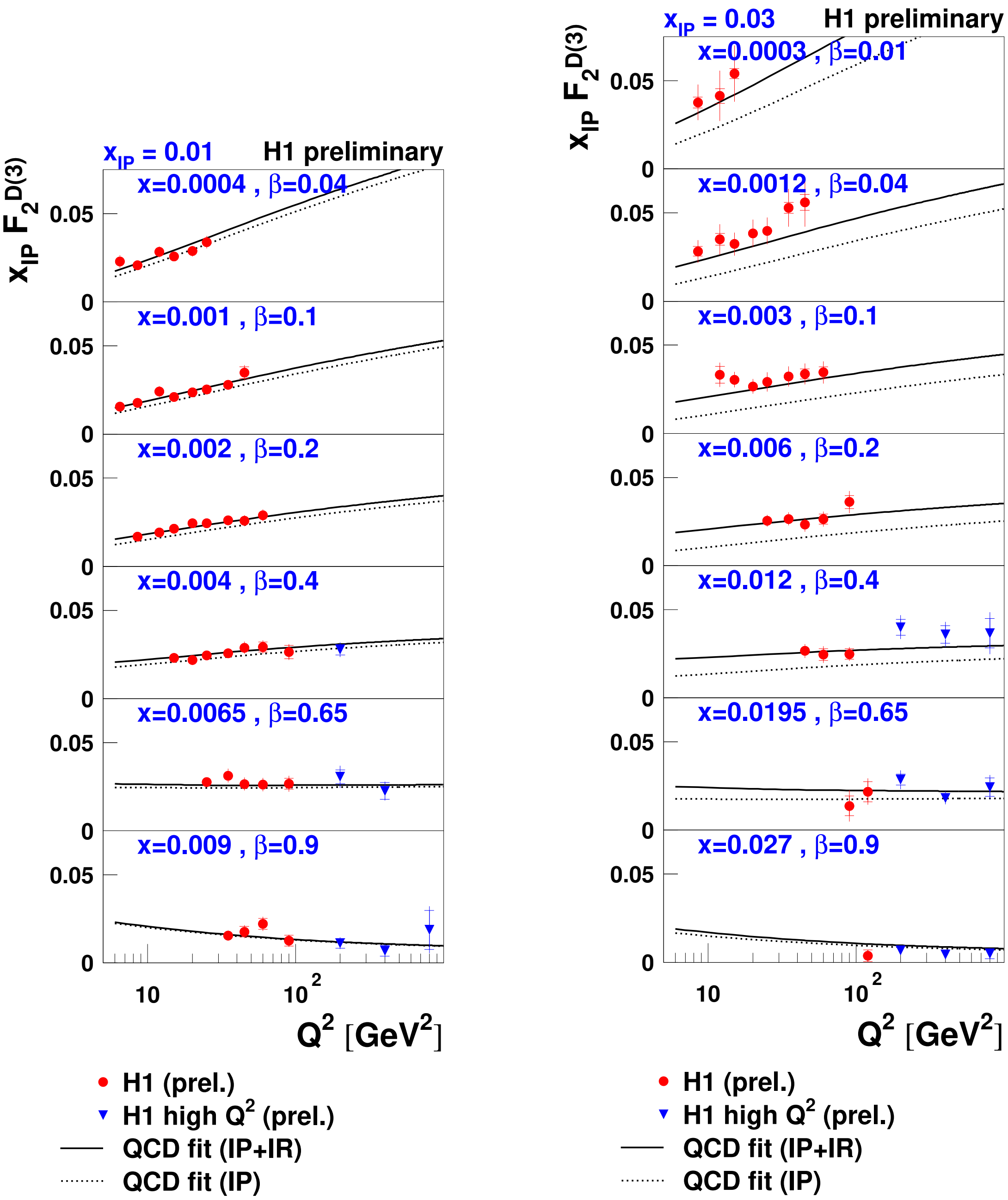

Figure 10: The measured diffractive structure function, plotted as $x_{I\!P} F_2^{D(3)}(\beta, Q^2, x_{I\!P})$ *(red filled circles)*, as a function of Q^2 for various values of β and at two fixed values of $x_{I\!P} = 0.01$ *(left)* and $x_{I\!P} = 0.03$ *(right)*. Also shown is the result of a QCD fit to the data as described in the text. The solid curves correspond to the sum of pomeron and sub-leading reggeon exchange contributions, whereas the dotted curves indicate the contribution from pomeron exchange only. For each value of β, the corresponding value of $x = x_{I\!P}\beta$ is indicated. In addition, the preliminary H1 data at high Q^2 [20] are shown *(blue triangles)*.

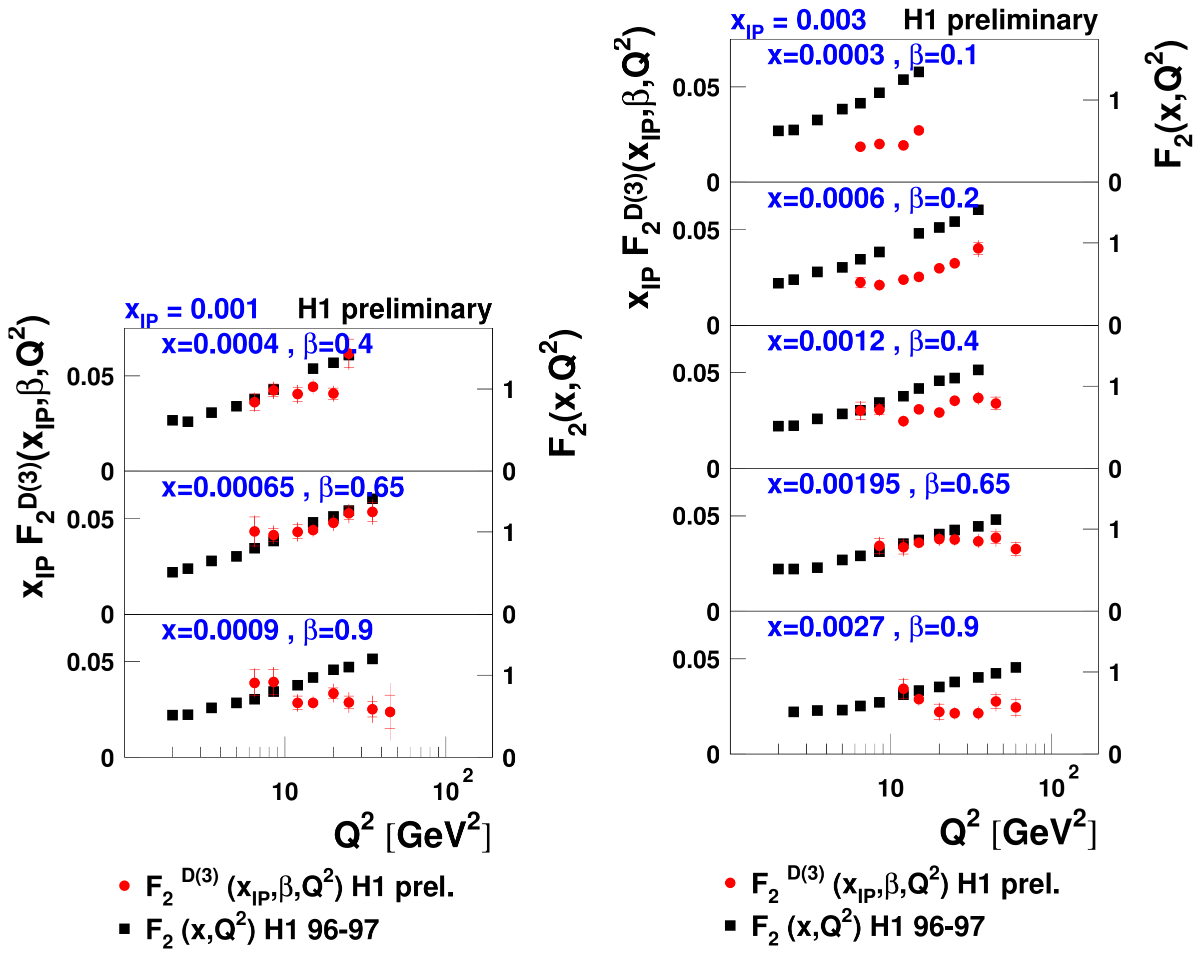

Figure 11: The measured diffractive structure function $x_{\mathbb{P}} F_2^{D(3)}(\beta, Q^2, x_{\mathbb{P}})$ *(red filled circles)*, plotted as a function of Q^2 for various values of β and at two fixed values of $x_{\mathbb{P}} = 0.001$ *(left)* and $x_{\mathbb{P}} = 0.003$ *(right)*. Also shown are $F_2(x, Q^2)$ data from [18] *(squares)*, where for each fixed $x = x_{\mathbb{P}}\beta$ the F_2 data points with x values closest to those of the F_2^D measurement are plotted.

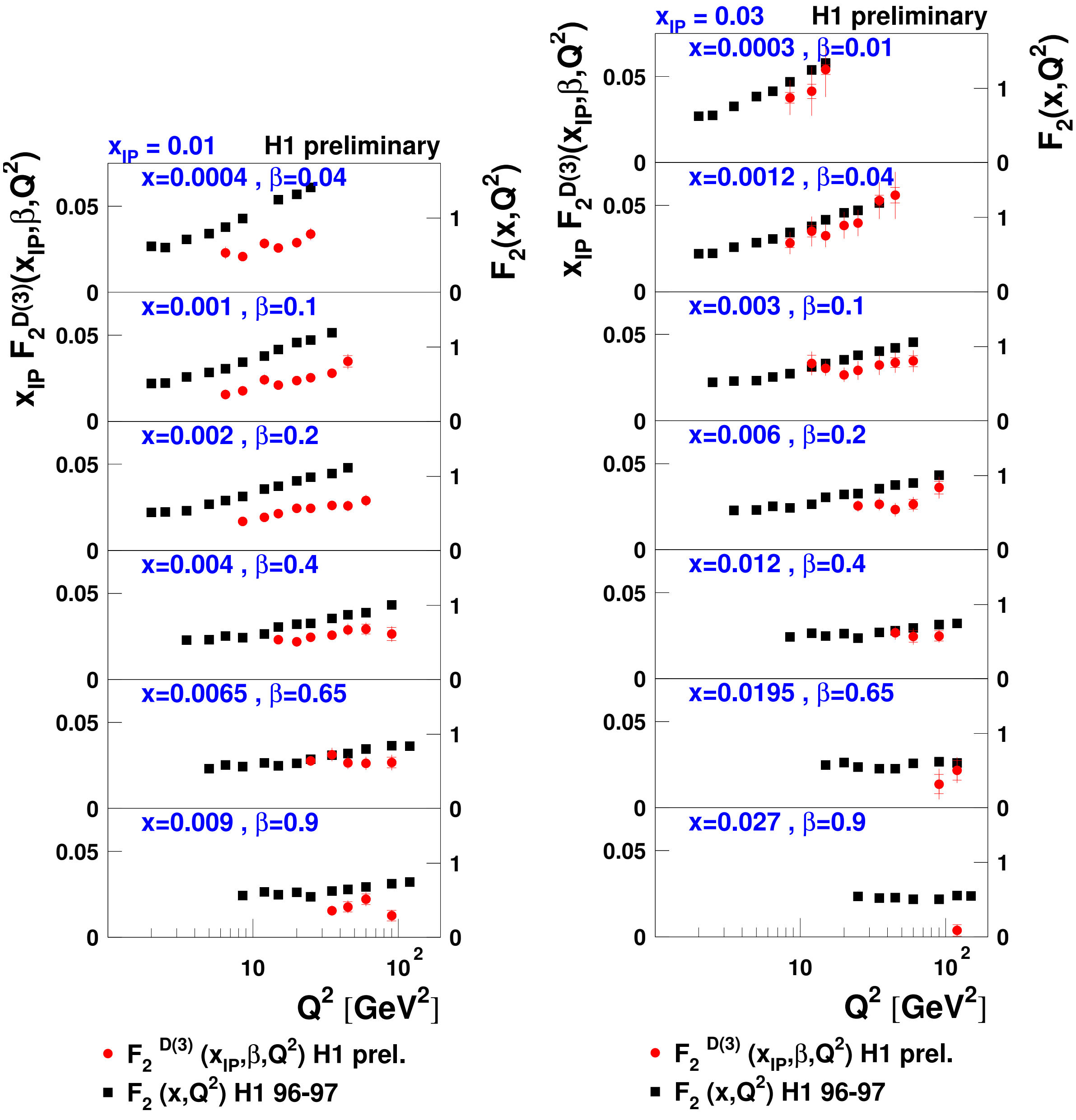

Figure 12: The measured diffractive structure function $x_{I\!P}F_2^{D(3)}(\beta,Q^2,x_{I\!P})$ *(red filled circles)*, plotted as a function of Q^2 for various values of β and at two fixed values of $x_{I\!P} = 0.01$ *(left)* and $x_{I\!P} = 0.03$ *(right)*. Also shown are $F_2(x,Q^2)$ data from [18] *(squares)*, where for each fixed $x = x_{I\!P}\beta$ the data points with x values closest to those of the F_2^D measurement are plotted.

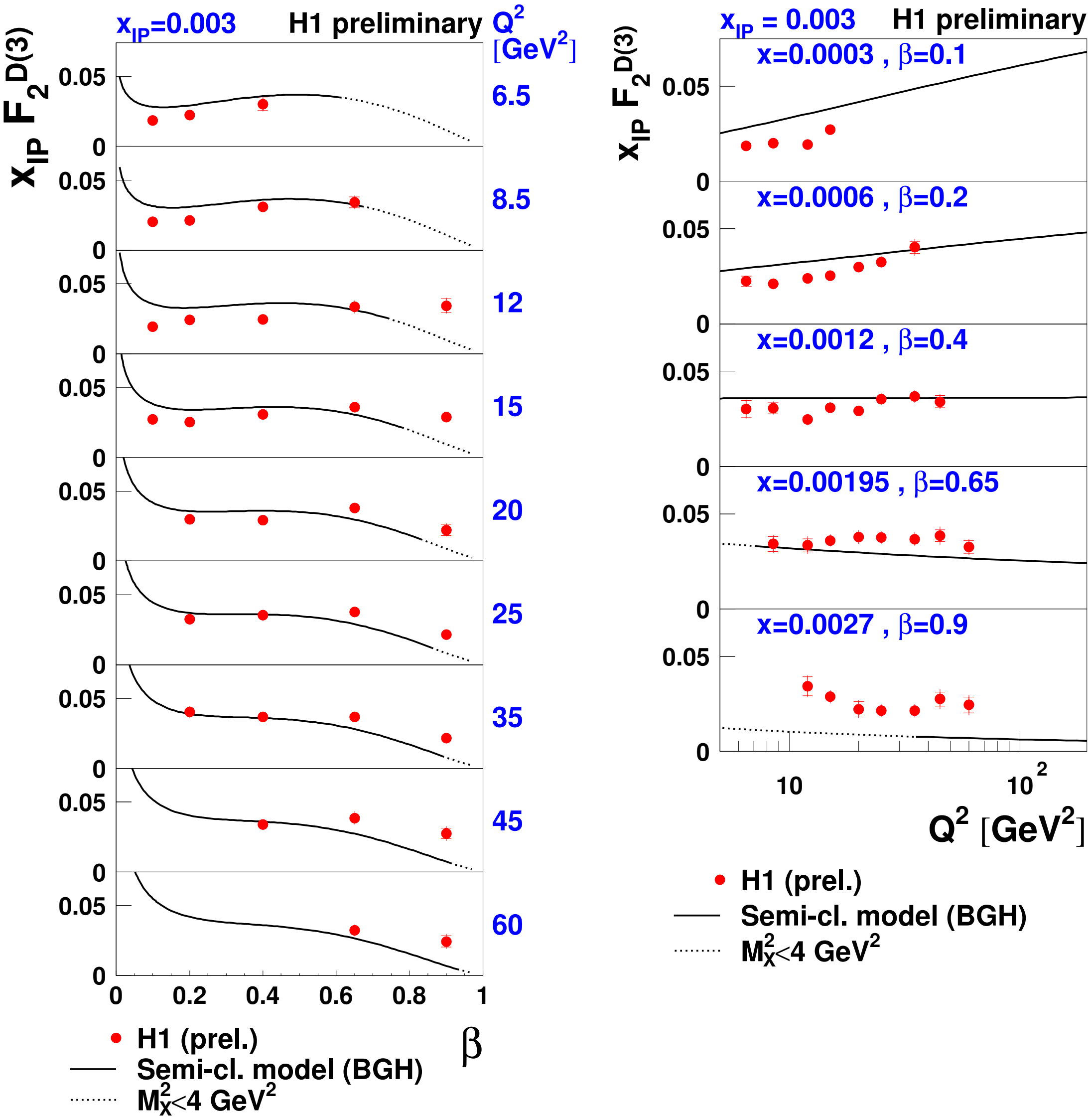

Figure 13: The measured diffractive structure function $x_{I\!P} F_2^{D(3)}(\beta, Q^2, x_{I\!P})$ *(red data points)* at fixed $x_{I\!P} = 0.003$, plotted as a function of β for various values of Q^2 *(left)* and as a function of Q^2 for various values of β *(right)*. The data are compared with the predictions of the semi-classical model by Buchmüller, Gehrmann and Hebecker [6] *(solid curves)*. The dotted curves correspond to an extension of the model into the region of small $M_X^2 < 4\ \mathrm{GeV}^2$, where the model is not expected to be valid.

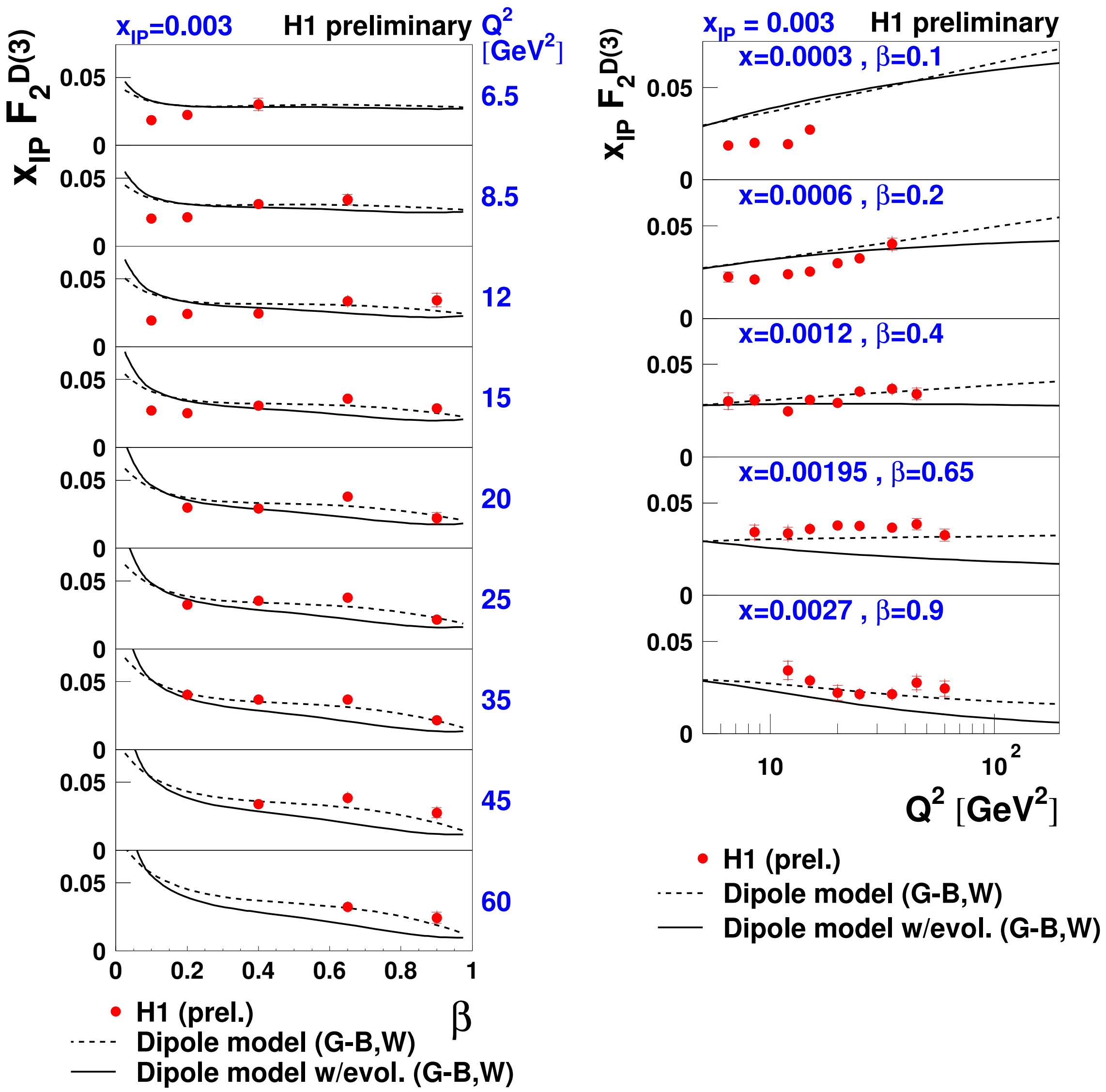

Figure 14: The measured diffractive structure function $x_{I\!P} F_2^{D(3)}(\beta, Q^2, x_{I\!P})$ *(red data points)* at fixed $x_{I\!P} = 0.003$, plotted as a function of β for various values of Q^2 *(left)* and as a function of Q^2 for various values of β *(right)*. The data are compared with the predictions of two versions of a colour dipole model by Golec-Biernat and Wüsthoff [7] *(dashed curves)* and [8] *(solid curves)*.

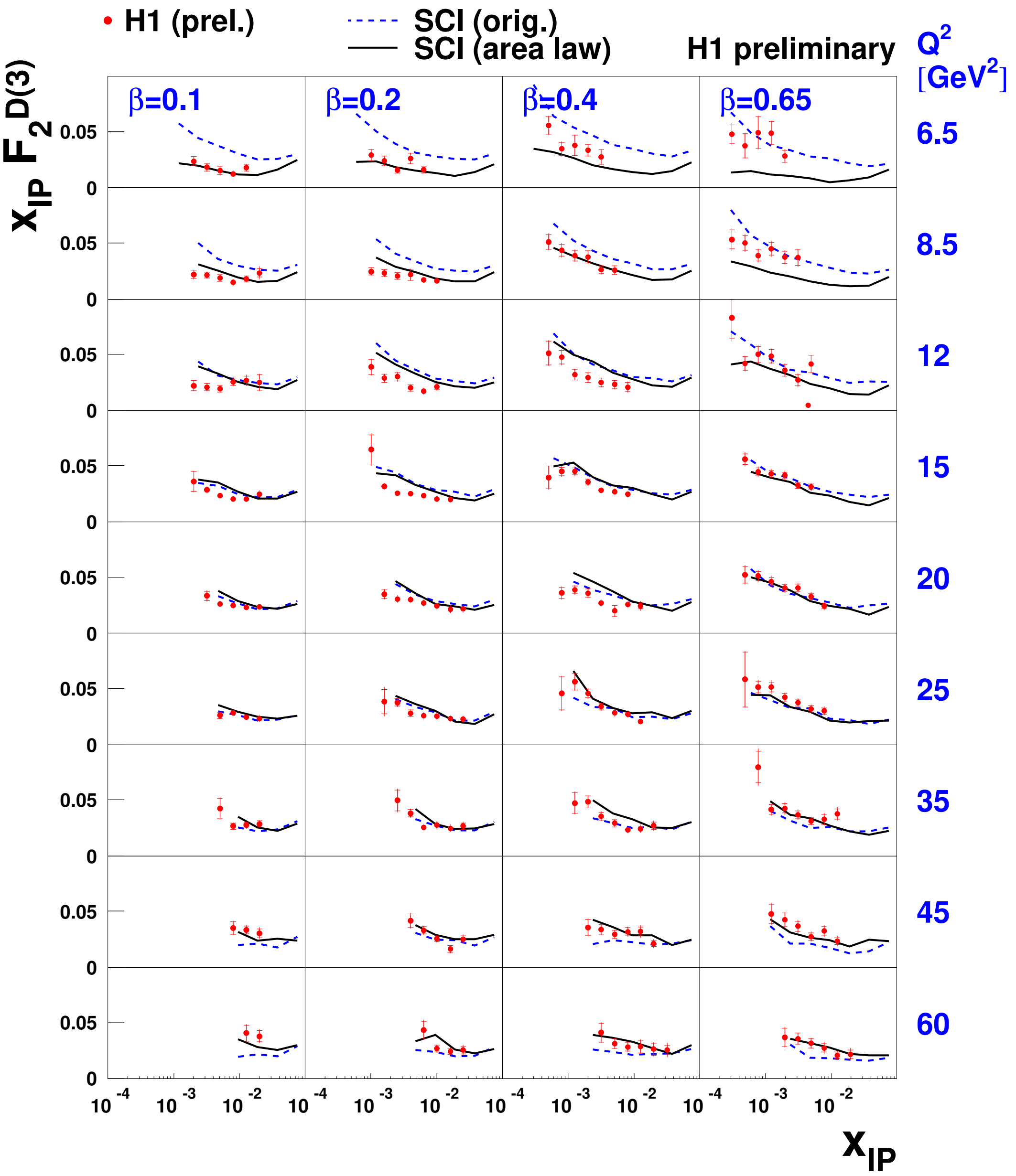

Figure 15: The measured diffractive structure function $x_{\mathbb{P}} F_2^{D(3)}(\beta, Q^2, x_{\mathbb{P}})$, plotted as a function of $x_{\mathbb{P}}$ at fixed values of Q^2 and β *(red data points)*. Only a sub-sample of the data, corresponding to $0.1 \leq \beta \leq 0.65$ and $Q^2 \leq 60\ \mathrm{GeV}^2$, are shown. The data are compared with the predictions of the original Soft Colour Interactions (SCI) model [21] *(dashed curves)* and its refinement based on a generalized area law [22] *(solid curves)*. The predictions have been obtained using the LEPTO $6.5.2\beta$ Monte Carlo generator [23].

Appendix

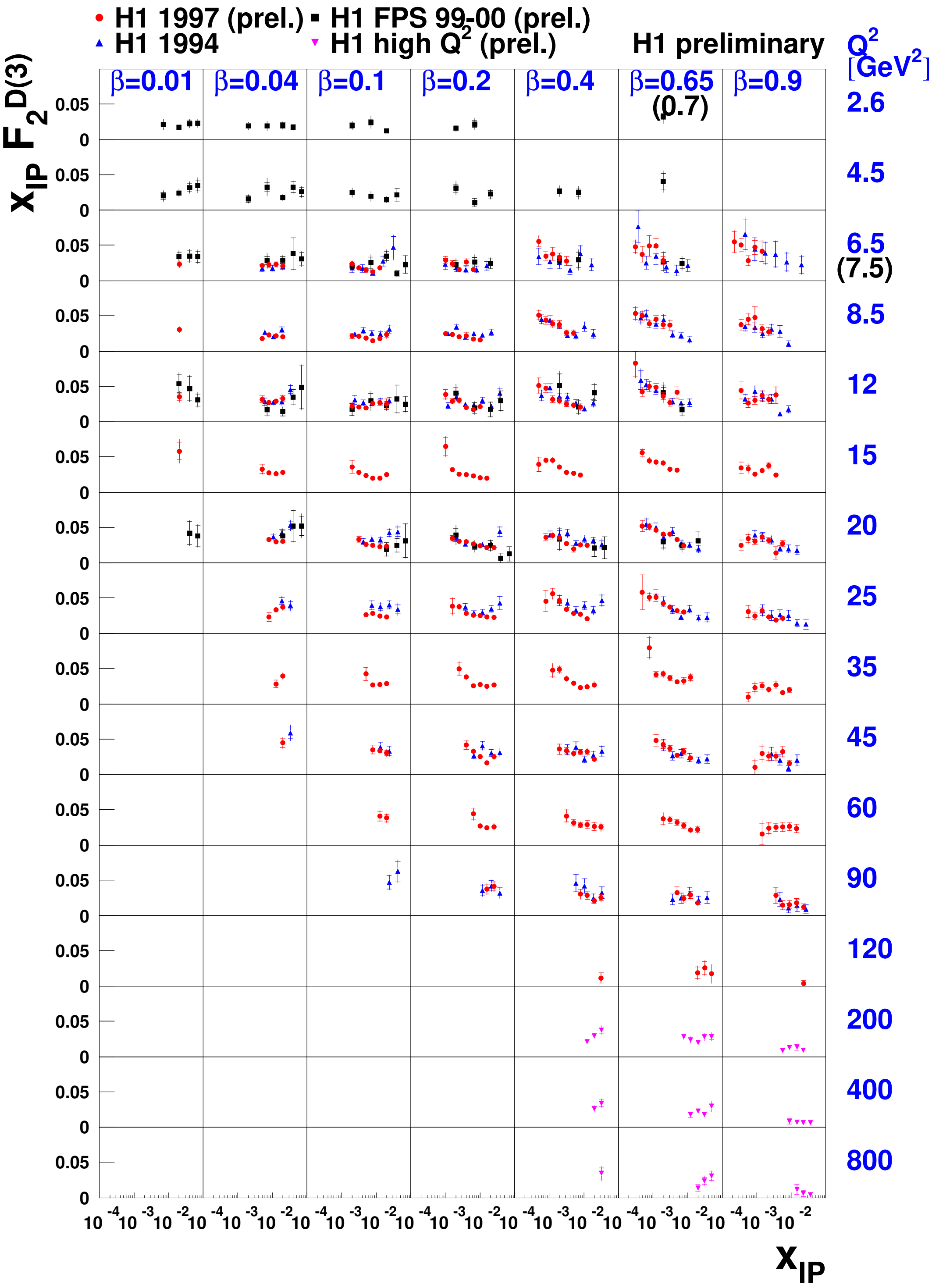

Figure 16: Summary plot of various H1 measurements of $F_2^{D(3)}$.

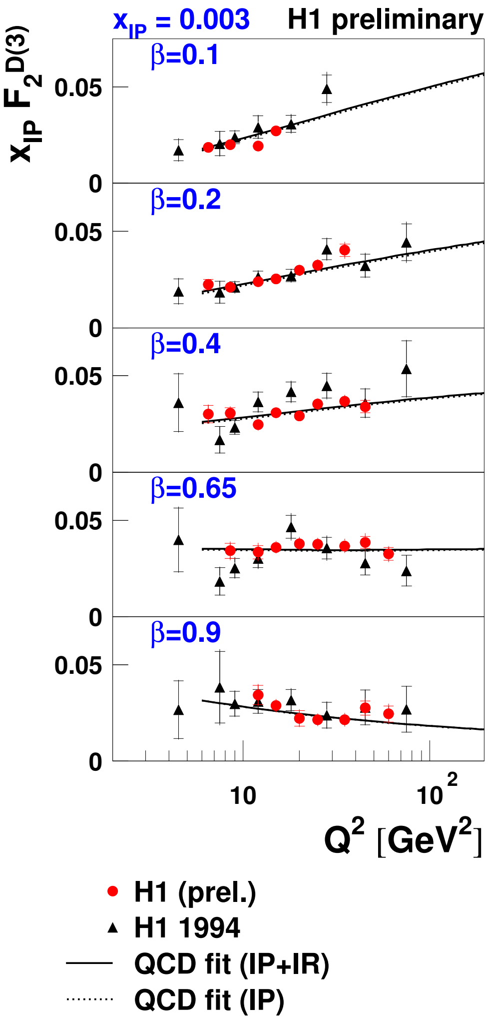

Figure 17: Q^2 dependence of $F_2^{D(3)}$ at fixed $x_{I\!P} = 0.003$, showing a comparison with the previous H1 measurement.

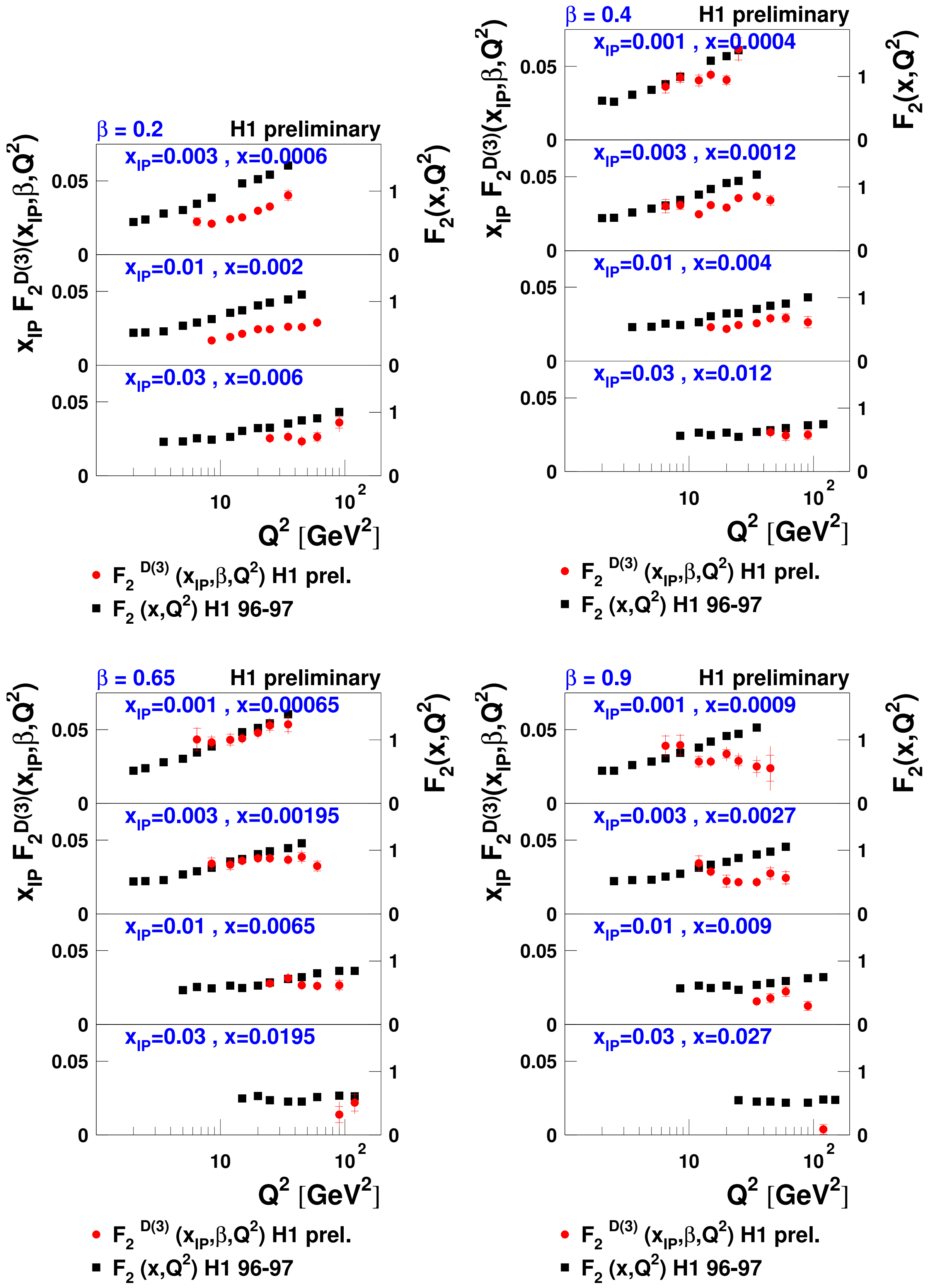

Figure 18: The Q^2 dependence of $F_2^{D(3)}$ as compared with $F_2(x, Q^2)$ at fixed $x = x_{I\!P}\beta$, grouping together available $x_{I\!P}$ points for a given fixed β value.

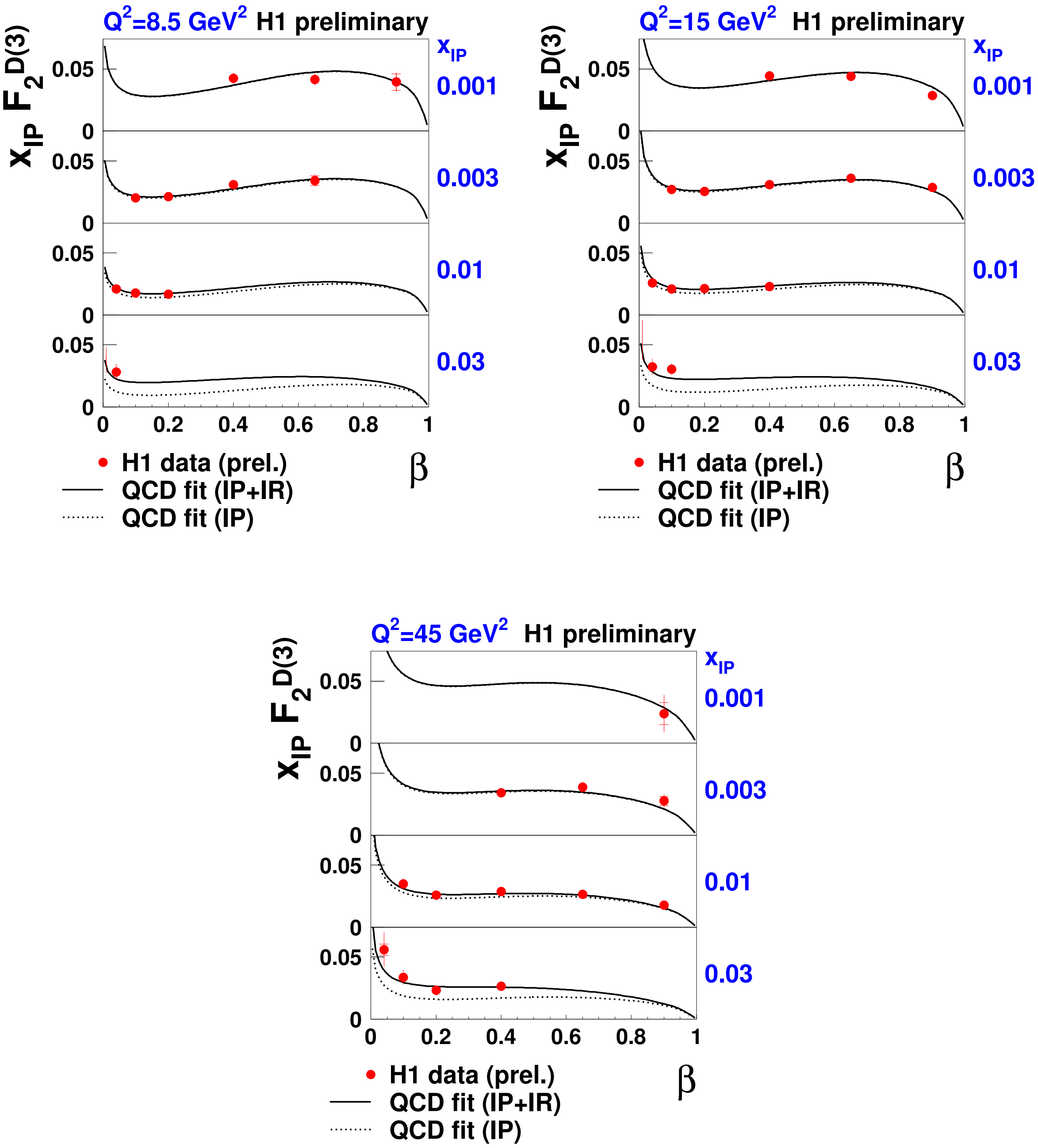

Figure 19: The β dependence of $F_2^{D(3)}$ at fixed Q^2, combining all four $x_{I\!P}$ bins.